Simulation Validation of Static and Forced Motion Flow Physics of a Canard Configured TransCruiser

Mehdi Ghoreyshi[*], Ramy Korkis-Kanaan[†], Adam Jirásek[‡]
Andrew J. Lofthouse[§], Russell M. Cummings[¶]

High Performance Computing Research Center, U.S. Air Force Academy

USAF Academy, Colorado 80840

The basic objective of this work is to validate CFD simulations performed on a transonic cruiser configuration called the TCR. The low speed aerodynamic characteristics of the TCR have previously been investigated at the Russian TsAGI T-103 wind tunnel as part of the European Framework 6 SimSAC project. The experimental results showed that static and dynamic pitch moment curves are very nonlinear. These experimental data are used in this work to validate CFD predictions with an overset grid approach. Two types of wind tunnel tests were conducted: static tests have been done for the angle-of-attack sweeps at zero degrees sideslip and the angle-of-sideslip sweeps at different angles of attack. Dynamic tests include forced sinusoidal oscillations in one of three modes of pitch, yaw, and roll. Both static and dynamic tests were conducted with/without a vertical tail and at different canard deflections. Dynamic tests are small- and large-amplitude motions with frequencies of 0.5, 1.0, and 1.5 Hz. CFD results were predicted with different turbulence models with a single mesh and an overset grid approach, and then compared with experimental data. The effects of the canard downwash flow on the wing aerodynamic performance are investigated. The comparison between the experimental and CFD simulations show that the results match well. The overset mesh with a gap between the canard and fuselage leads to the same predictions as the single grid (without a gap). CFD solutions show that vortices are formed over the canard, fuselage, LEX, wing, and the vertical tail (at sideslip angles). Each vortex appears to have a primary vortex accompanied by a smaller counter-rotating secondary vortex. These vortices are influenced by the canard presence and deflection. At high angles of attack, the canard vortex has two favorable effects in terms of increasing the maximum lift and delaying the wing vortex breakdown. In the range of angles of attack between 18° to 24°, the LEX and wing vortices interact and then merge, leading to a sudden change in the slopes of force and moment curves. Finally, CFD data show that increasing the canard angle produces a stronger vortex over the canard, but smaller fuselage and LEX vortices.

Nomenclature

A_0	motion amplitude, rad
a	speed of sound, m/s

---

[*]Senior Aerospace Engineer, Corresponding author: Mehdi.Ghoreyshi@usafa.edu
[†]Aeronautical Cadet
[‡]Research Fellow
[§]Director
[¶]Professor of Aeronautics

American Institute of Aeronautics and Astronautics

b	wing span, m
C_D	drag coefficient, $D/q_\infty S$
C_N	normal-force coefficient, $N/q_\infty S$
C_{Mx}	roll moment coefficient, $M_x/q_\infty Sb$
C_{My}	pitch moment coefficient, $M_y/q_\infty Sc$
C_{Mz}	yaw moment coefficient, $M_x/q_\infty Sb$
C_p	pressure coefficient, $(p - p_\infty)/q_\infty$
C_Y	side-force coefficient, $Y/q_\infty S$
c	mean aerodynamic chord, m
D	drag force, N
f	frequency, Hz
N	normal force, N
M_x	roll moment, N-m
M_y	pitch moment, N-m
M_z	yaw moment, N-m
M	Mach number, V/a
p	static pressure, Pa
p_∞	freestream pressure, Pa
q_∞	dynamic pressure, Pa, $\rho V^2/2$
Re	Reynolds number, $\rho V c/\mu$
S	Planform area, m^3
V	freestream velocity, m/s
x, y, z	aircraft position coordinates

Greek

α	angle of attack, rad
$\dot{\alpha}$	time-rate of change of angle of attack, rad/s
β	side-slip angle, rad
ϕ	control surface deflection, rad
ρ	air density, kg/m^3
μ	air viscosity, kg/(m.s)

Subscripts

c	canard
w	wing

I. Introduction

The computational fluid dynamics(CFD) simulations are anticipated to become the primary tool in the design of modern commercial and military aircraft. The traditional handbook methods and low-fidelity aerodynamic tools fail to predict accurately the aerodynamic behavior over an extended flight envelope and/or of a novel configuration.[1] The flight tests are expensive, sometimes require risky maneuvers, and become available late in the design cycle. As a result, CFD predictions and wind tunnel experiments play a crucial role in the development of modern aircraft prior to fabrication. Specifically, CFD has become reliable enough to detect the source of undesirable flight characteristics experienced in the flight testing.[2] This ensures the early availability of high quality aerodynamic models for design of control system and minimizing risk and uncertainty in a new airplane product. However, CFD techniques are subject to inaccuracies and must be validated and evaluated on the basis of experimental data. This work considers the application of CFD modeling to predict static and forced motion aerodynamic responses of a canard configured TransCRuiser named the TCR.

The TCR (shown in Fig. 1 (a)) is a concept design of a civil transport aircraft operating at transonic speeds with the cruise Mach number of 0.97.[3] The design was proposed by the Swedish aerospace company

American Institute of Aeronautics and Astronautics

SAAB; the initial concept was examined and modified within the European Framework 6 SimSAC project.[4] The final TCR aircraft is a canard-wing-vertical tail configuration and includes a wing leading edge extension (LEX). The canard is an all moving surface and a close-coupled type. Both the wing and canard are swept back by 60° causing vortex formation at moderate to high angles of attack. The transonic design speed was chosen to highlight the shortcomings of the handbook methods and linear aerodynamic codes available in the SimSAC project. Even at low subsonic speeds, the aircraft has very nonlinear aerodynamic behavior due to canard/wing interference effects.[1,5,6] The presence and deflection of the canard will affect the wing performance, specifically for a close-coupled canard configuration.[7] As a result, the TCR aircraft provides a challenging task for CFD simulation.

For validation of CFD models, TCR predictions are compared against available wind tunnel measurements of the SimSAC project. The wind tunnel model was built at Politecnico di Milano in Italy and then tested in the TsAGI T103 wind tunnel in Russia at low speed and up to high angles of attack. Several configurations were investigated to allow consideration of the influence of single components (vertical tail and canard) on the overall performances. The static tests included a variation of side-slip angles, angles of attack ranging from -10° to 40° with step of 2°, and the canard deflections from -30° to 10° with step of 5° and an asymmetric deflection with -10/+10 degrees. Dynamic tests are small- and large-amplitude motions with motion frequencies of 0.5, 1.0, and 1.5 Hz and were tested in pitch, roll, and yaw modes. For small amplitude motions, dynamic derivatives were estimated using a linear regression method and available in the experimental data.[8] In addition, TCR was tested for plunged forced oscillations to measure $\dot{\alpha}$ derivatives.

In the experiments, the left and right canard panels were deflected in eight different positions including an asymmetric position. Regeneration of the grid for all these cases can be a very time-consuming and labor-intensive task. This work investigates the use of an overset method for modeling the TCR canard deflection because an overset mesh allows large displacements and surface deflections. In an overset method, independent meshes are generated around different body elements and then the discretized flow equations are solved using an interpolation technique. The results of the overset mesh are compared with experimental data and those predicted by a single mesh at canard angle of zero degrees. This allows investigating the effects of the gap that exists between the canard and fuselage of the overset mesh on the aerodynamic predictions.

The computational results of this work will aid in the understanding of the flowfield over TCR. Specifically, the TCR wind tunnel experiments only provide total integrated forces and moments; surface pressure measurements and flowfield information are not available. In addition, the load balance used in the wind tunnel could not measure the drag force. In the wind-tunnel experiments, the canard and wing interference effects could be measured by using pressure taps for canard on and off configurations, for example see the work of Er-El.[9] However, these measurements will add to the cost of experiments. The surface flow conditions are easily available in CFD simulations; forces and moments could also be isolated for each surface/region of interest to study the canard/wing interference. Note that the TCR wind tunnel experiments took about three years to plan, build the model, and complete all the tests.

There are three objectives in the present study: 1) to contribute to the understanding of the flow physics of the TCR configuration, 2) to develop validated aerodynamic models for the TCR using an overset grid method 3) and to investigate the effects of the canard downwash flow on the wing aerodynamic performance. The work is organized as follows: the first section reviews the canard-wing interaction effects. Next, the TCR geometry and mission requirements are detailed. The computational grids are presented in the next section. A basic introduction of the CFD flow solver is also provided. The results are then presented and discussed, followed by the concluding remarks.

II.   Canard-Wing Interaction

A canard-wing configuration is an attractive design choice for a high-speed, highly maneuverable aircraft.[10] The presence of a vortex generating surface ahead of the wing increases the maximum lift, reduces the trim drag, delays the wing stall, and improves the maneuverability.[11] While a conventional aircraft should generate some negative lift on the tail to balance the wing pitch moment around center of gravity, the canard will produce an upward lift. The main wing of a conventional aircraft should compensate the tail negative lift causing the induced and trim drag to increase as result of increased lift.[12] A canard offers two possible benefits with reducing the wave drag: first it improves the longitudinal variation of the cross-sectional area particulary for a close-coupled canard,[11] the second benefit is that it makes an aerodynamically

American Institute of Aeronautics and Astronautics

clean fuselage aft section compared to a tailed configuration.[13]

A properly designed and placed canard will stall before the main wing and as a result, the airplane nose drops (an uncommanded pitch) which prevents the main wing from entering the stall regime. In addition, the canard provides a positive pitch control which could counteract the nose down tendency of the airplane as it enters the transonic regime("Mach tuck"). Finally, the canard improves the stall/spin recovery.

The canard is a statically destabilizing device because of its location ahead of the center of gravity.[14] As a result the canard size should be as small as possible to minimize its destabilizing effect, however, this decreases the pitch control effectiveness as well.[12] Canard-wing configurations could be classified into long-coupled and close-coupled as shown in Fig. 2. Roskam[15] suggested the ratio between the distance between canard (mean aerodynamic center) and the wing (mean aerodynamic center) to the mean aerodynamic chord to classify airplanes into long-coupled and close-coupled types; while a long-coupled airplane has a ratio greater than five, a short-coupled typically has a ratio less than three.

If the design focus is on reducing aircraft drag at cruise conditions, the canard should be placed far ahead of the wing. This configuration minimizes the canard-wing interference effects and requires a smaller upward load on the canard; both effects would help to reduce the trim drag.[10] An aircraft example is X-31 which has canards that deflect between +20 and -70deg for pitch control requirements.[16] The problems related to a long-coupled configuration are mainly stability issues. Torenbeek[10] stated that the size of a long-coupled canard should be less than 10% of the main wing to achieve stability. This makes a long-coupled canard the primary pitch control surface rather than a lifting surface. Therefore a long-coupled canard typically requires large deflections for the pitch control.

The canard/wing interactio for a short-coupled canard increases the maximum lift and drag in comparison to a long-coupled canard. Examples of the close-coupled configurations are NASA X-29, SAAB Viggen and Grippen, and European Fighter Aircraft. Typically, close-coupled canards are bigger than long-coupled ones, and therefore they are lifting surfaces as well as a control surface.[17] These highly-loaded surfaces will produce excessive drag as well. At small angles of attack, the canard induces a downwash over the wing within the canard span and an upwash outside its span.[18, 19, 17] As a result, while the flow tends to remain attached over the wing behind the canard, it tends to separate outside the canard.[17] Although, this leads to a lift loss on the wing compared with a wing only configuration, the overall aircraft lift will be identical to a canard-off configuration due to increased lift by the canard. Oleary[17] stated that "at low angles of attack ($< 10°$) the lift-curve slope of a model with or without a canard is identical."

For slender delta canard/wing surfaces, the flow at moderate to high angles of attack is characterized by two large counter-rotating primary vortices formed over the upper surface. The sharp leading edges of slender wings cause the boundary layer to separate and the separated shear layers to roll up into vortices. The shear layer may exhibit instabilities that increase the vortical substructures and, therefore, the vortices increase in both size and strength as it extends downstream. A close-coupled canard has favorable interference between the canard and wing leading-edge vortices.[17] In these configurations, the canard vortex helps to delay the wing vortex breakdown to higher angles compared with a wing only configuration. As a result, a canard-on delta wing has larger maximum lift coefficient than a canard-off configuration.[20]

III.   Test Case

The TCR, developed by SAAB, is a concept design of a civil transport aircraft operating at transonic speeds. The concept features a low wetted area, fuel efficiency at transonic cruise, low noise radiation, relaxed static stability boundaries, and low maneuver and trim drag.[8] The design specifications are detailed by Eliasson et al.,[5] with some examples are given below:

Payload: Nominal design for 200 passenger in economy class

Design Cruise Speed: $M_D = 0.97$ at an altitude at or above 37,000 ft.

Range: 5,500 nm, followed by 250 nm flight to an alternate and 0.5 hour loiter time at an altitude of 1,500 ft. Additional 5% of block fuel.

Take-off and landing: Take-off distance of 8858 ft at an altitude of 2,000 ft, ISA+15 and maximum take-off weight. Landing distance of 6561 ft at an altitude of 2,000 ft, ISA and maximum landing weight with maximum payload and normal reserves.

American Institute of Aeronautics and Astronautics

Power plants: Two turbofans

The initial concept by SAAB was a conventional tailed configuration. Its design study revealed that a very large horizontal tail deflection should be applied to trim the aircraft at the design point.[1] The initial design was then investigated further within the SimSAC projects to improve the aircraft stability and control characteristics; the final design became a canard-wing-vertical tail configuration as shown in Fig. 1 (a).

The TCR canard is an all-moveable control surface and the primary pitch control device for the aircraft. The canard exposed area is about 15 percent of the wing reference area. The apex positions of the wing and canard are at 0.26 and 0.12 in fraction of the total fuselage length,[1] making the canard a close-coupled type.

A wind tunnel model was next designed and built to one-fortieth scale by Politecnico di Milano. The wind tunnel model layout and dimensions are shown in Fig. 3. The authors did not find the TCR airfoil information, however, so the canard has a symmetric airfoil and the wing airfoil section at $Y = 0.3m$ was extracted from the CAD as shown in Figure 4. Other geometry parameters are given in Table 1.

Note that the TCR main wing has a round (blunt) leading edge. The vortical flow behavior over slender wings with a blunt leading edge is very different from those of sharp leading edges.[21,22] For blunt wings, the vortex flow structure is very complicated and depends heavily on the leading edge bluntness and the wing sweep angle.

Table 1. TCR wind tunnel model parameters

Parameter	Values
Wing area, S_w	0.3056 m^2
Canard area, S_c	0.045 m^2
Wing span, b_w	1.12 m
Canard span, b_c	0.3 m
Mean aerodynamic chord, c	0.2943 m
CG position form the aircraft nose, x_{CG}	0.87475 m
Total fuselage length	1.597 m
Fuselage Diameter	0.925 m

IV.   Computational Grids

Half- and full-geometry meshes are available, corresponding to the TCR wind tunnel model with and without the canard. The RANS meshes were generated in two steps. In the first step, the inviscid tetrahedral mesh was generated from a clean configuration using the ICEMCFD code. The inviscid mesh was then used as a background mesh by TRITET[23,24] which builds prism layers using a frontal technique. TRITET rebuilds the inviscid mesh while respecting the size of the original inviscid mesh from ICEMCFD. Symmetric meshes are shown in Fig. 5 for the TCR model with and without canard. The symmetric grid without the canard has 26 Million cells and the mesh with the canard contains 33 million cells.

Wind tunnel experiments were run for the canard deflection angles ranging from -30° to 10° with a step of 5°. An overset grid approach is used in this work for simulating the canard deflections. The overlapping grids were generated individually for the body and canard, without the need to force grid points aligned with neighboring components. However, a grid assembly approach requires some gaps between the canard and the body. The grid also needs to be refined around the gaps which often makes the grid size larger than a single grid. In this work, two hybrid RANS meshes were generated from the half and full geometry models of the TCR without canard surfaces. The grids for left and right canards were generated separately and overset onto the main grid. The background and minor overset grids were also generated using the ICEMCFD and TRITET codes. The assembled grid of the half geometry has about 40 million cells; the overset grid at a canard deflection of -30° is shown in Figure 6.

American Institute of Aeronautics and Astronautics

V. Experimental Setup

The TCR wind-tunnel model was built with a geometric scaling factor of 1 : 40 of the actual size to fit the size requirements of the TsAGI subsonic wind tunnel. This wind tunnel has an open jet working section of the continuous type with an elliptical cross section of 4.0×2.33m.[8] The wind tunnel can operate at velocities up to 80 m/s and Reynolds numbers up to 5.5 million. For the dynamic tests, the model was mounted on a platform driven by actuators. The model center of gravity was located along the fuselage center line at 54.78% of the total length from the foremost point. The moment reference point and the center of oscillatory motion coincide with this point. Figure 1 (b) shows the TCR wind tunnel model at the TsAGI subsonic wind tunnel; note that there is a gap region between the canard and the fuselage.

The normal and lateral forces and the moment coefficients from static and large amplitude pitch oscillations were measured. The mean values, in-phase and out-of-phase components of the force and moment coefficients were also measured from the rotary and oscillatory motions. All tests were run at a free-stream speed of 40 m/s, which corresponds to a sea level Mach number of 0.117, and a Reynolds number of 0.778 million based on the mean aerodynamic chord of the wind tunnel model. These experimental data can be obtained from the SimSAC project website (http://www.ceasiom.com) and are used in this work to validate the overset grid approach and Cobalt CFD solver used at the U.S. Air Force Academy (USAFA).

VI. CFD Solver

The flow solver used for this study is the *Cobalt* code[25] that solves the unsteady, three-dimensional and compressible Navier-Stokes equations in an inertial reference frame. The ideal gas law and Sutherland's law close the system of equations and the entire equation set is nondimensionalized by free stream density and speed of sound.[25] The Navier-Stokes equations are discretised on arbitrary grid topologies using a cell-centered finite volume method. Second-order accuracy in space is achieved using the exact Riemann solver of Gottlieb and Groth,[26] and least squares gradient calculations using QR factorization. To accelerate the solution of the discretized system, a point-implicit method using analytic first-order inviscid and viscous Jacobians is implemented. A Newtonian sub-iteration method is used to improve time accuracy of the point-implicit method. Tomaro et al.[27] converted the code from explicit to implicit, enabling Courant-Friedrichs-Lewy numbers as high as 10^6. Some available turbulence models are the Spalart-Allmaras model,[28] Wilcox's k-ω model,[29] and Mentor's SST model.[30]

Cobalt uses an overset grid method which allows the independent translation and rotation of each grid around a fixed or moving hinge line. In this method, overlapping grids are generated individually, without the need to force grid points aligned with neighboring components.[31] In Cobalt, the overlapping grids are treated as a single mesh using a grid-assembly process. This includes a hole-cutting procedure in overlapping regions and interpolation between overlapping grids. The translation and rotation of overset grids around the hinge line are input to the code using a Grid Control File (GCF). The hinge line is defined by a reference point and a vector combination. The rotations are based on the right-hand rule and consist of angles in an order of pitch, yaw, and roll angle. These angles are estimated from the deflection angle of a control surface and the relative angles between the hinge line and grid coordinate axes.

VII. Results

In all subsequent simulations, the free-stream velocity is 40m/s and Reynolds number corresponds to 0.778 million based on the mean aerodynamic chord. All simulations were run on the Department of Defense High Performance Computing Modernization Program (HPCMP).

The turbulence modeling and grid sensitivity results are not included here. Briefly, they showed that the SA turbulence model with Rotation Correction (SARC) match the experimental results better than the SA model in most angles of attack. Specifically, the SARC model has been successfully used in aerodynamic prediction of aircraft with vortical flows, at least before the appearance of vortex breakdown. In addition, the grid sensitivity results showed that the predictions from all girds converged to those predicted by the finer grids.

First, validation results are shown in Fig. 7 for the angle-of-attack sweeps at zero degrees of sideslip. CFD simulations were performed on the single grids with and without the canard; in the former, the canard is not deflected, i.e. $\phi_c = 0°$. All solutions were run up to 4,000 iterations, achieving a density residual drop

American Institute of Aeronautics and Astronautics

of three orders of magnitude. Normal force, pitch moment, and drag force were time-averaged over the last 500 iterations and were compared with the TCR experimental data in Fig. 7. Note that the drag force was not measured in the wind tunnel experiments.

Figure 7 shows very good agreement between Cobalt predictions and the experimental results for both canard on and off configurations. For angles of attack less than eight degrees, the canard presence has no significant effects on the aircraft normal force (lift) and drag. At higher angles, however, the canard-configured TCR shows higher normal force and drag values. The pitch moment curves have different slopes for the canard on and off geometries; the pitch moment values only match at zero degrees of angle of attack and are different elsewhere. The canard is a destabilizing device and causes a less negative (or more positive) total pitch moment as shown in Fig. 7(b).

A detailed assessment of the plots of Fig. 7 show that dips can be observed in the CFD normal-force coefficients for the canard on and off configurations; the dips are located at angles of attack between 18° to 24°; the dip becomes smaller in the presence of the canard. Small dips can also be seen in the drag force plots at the same angles. The pitch moment slope of the canard-off geometry is negative and then becomes nearly zero for angles above 28°; there is a sudden change in the slope for angles between 18° to 24°. On the other hand, the pitch moment slope in the presence of the canard becomes positive around 12°; it becomes negative for angles between 20° to 24° and again takes positive values, though they are small.

The CFD results of Fig. 7 may raise the question as to why CFD shows a dip in the plots but not the experiment? An answer to this question might be found be assessing Fig. 7 (d) which shows the CFD normal force of the canard-off geometry for a sweep of angle of attack with different run times. The results show that no dip or a very small dip can be seen in the plots if the solutions only run for 2,000 iterations. The solutions at 2,000 iterations have already reached the steady-state values for most angles, but they still change for angles between 18° to 24° with more iterations. A dip will be formed in the plots by iterating solutions up to 4,000. More run time, however, do not make much difference from the solutions found at 4,000 iterations. This confirms that solutions at these angles need enough time to converge and stabilize. Unfortunately, the wind tunnel details (time run at each angle) are not available to comment on the experimental data.

To better understand the canard and wing contributions to total forces and moments, Fig. 8 shows the lift, drag, and pitch moment coefficients for individual surfaces. Figure 8(a) shows that at small angles of attack, the wing in the presence of the canard has less lift than a wing-only configuration; this is mainly due to canard downwash effects on the wing. However, the total lift remains the same because of the additional lift generated on the canard. At higher angles the wing behind the canard produces more lift than a wing-only geometry because of the canard vortex effects on the wing. These vortices will increase wing drag as well. Figure 8(a) shows that the canard stalls earlier than the main wing. Dips can again be seen in the wing plots. Figure 8(b) shows that the canard pitch moment slope is positive for all angles, confirming that the canard is a destabilizing surface. The wing pitch moments (with and without canard) match with each other at small angles of attack and have negative slopes for most angles.

Figure 9 details the canardless TCR flow solutions at different angles of attack and zero sideslip angle. For several x positions, iso-surface of vorticity magnitude were created and colored by the vorticity magnitude. The boundary layer thickness is related to the diffusion of vorticity generated on the surface. The vorticity isosurfaces of Fig. 9 become thicker in the streamwise direction as the boundary layer grows. The solutions also show that the boundary layer over the fuselage is much thicker than the wing boundary layer, possibly due to a longer fuselage section and the sharp angle between the fuselage nose cone and fuselage cylindrical section (see Fig. 3). Apart from the boundary layer growth, no other feature of interest was found for TCR solutions below 6° angle of attack.

At 6° angle of attack, the canardless TCR shows a wing tip vortex starting at about quarter chord of wing tip. Note also that small vortices are formed over the wing starting at different wing leading edge sections (but do not originate from the wing apex) as shown in Fig. 9(a). As the angle of attack increases, these vortices become bigger and stronger, they move inboard and the starting point moves towards the wing apex. At $\alpha = 12°$, an outboard vortex is formed over the wing originating form the wing apex. This vortex interacts with the wing tip vortex. Also, an inboard vortex is formed which originates from the LEX. Both of these vortices have a vortex structure containing a primary and small counter-rotating secondary vortex. These vortices can be seen in Fig. 9(b). In addition, the boundary layer over the fuselage separates and rolls into two counter-rotating vortices.

Further increase in the angle of attack makes all vortices stronger. The outboard vortex still emanates from the wing apex and travels downstream, however its core begins to move towards the inboard (LEX)

American Institute of Aeronautics and Astronautics

vortex with increased angle of attack. At 16° angle of attack, a portion of the inboard vortex is being sucked under the outboard vortex. At $\alpha = 18°$ the inboard and outboard vortices interact and merge downstream as shown in Fig. 9(c). Only one wing vortex travels downstream. As the angle of attack increases further, the outboard vortex still moves inboard and the merging point shifts upstream. The vortex core locations and the merge point do not change much after $\alpha = 24°$. The dips seen in the normal force and drag force of Fig. 7 are related to the interaction and merging of vortices at angles between 18° to 24°. For higher angles, the merged vortex becomes bigger but the merging point does not change much. For example, Figs. 9(d)-(e) show the vortices at 24° and 30° angles of attack, respectively. These figures show that the vortex core position and the merging point are still the same, however, the vortices have different sizes. At higher angles, the fuselage vortex interacts with the LE vortex as well as the merged vortex. This can be seen in Fig. 9(f) for 40° angle of attack.

Likewise, Figs. 10 and 11 detail the canard-configured TCR flow solutions at different angles of attack and zero sideslip angle. Comparing with canardless solutions, Fig. 10(a) shows that at $\alpha = 6°$, the wing flow solutions of the canard on and off configurations are very similar. Figure. 10(a) also shows that a tip vortex is formed over the canard. At $\alpha = 12°$, the starting point of canard vortex is at the canard apex. Due to canard downwash and upwash effects, the wing solutions for canard on and off are slightly different. The wing in the presence of the canard shows smaller inboard and fuselage vortices than the canardless configuration; this is due to canard downwash effects that reduce the local angle of attack behind the canard span. On the other hand, the wing outboard vortex is slightly bigger in the presence of the canard.

Figure 10 shows that the canard vortex becomes bigger with increasing angle of attack. At $\alpha = 18°$, the wing vortices merge, but the inboard vortex is much smaller for the canard-configured than the canardless geometry. For higher angles, the TCR canard has favorable effects on the wing aerodynamic performance. At 24° angle of attack, the wing behind canard has a stronger merged vortex than the wing-only configuration. This can be seen in Figs. 10(d) and 11(d); this is mainly due to canard upwash outside the canard span. This leads to more negative pressure region over the wing surface, higher lift, and delayed vortex breakdown. Note that the fuselage vortex is still small for the canard-configured TCR because of downwash effects behind the canard span.

The sideslip sweeps were simulated using the full-aircraft mesh with zero canard angle; the sideslip angle ranges from -16° to 16° and corresponds to two angels of attack of 6° and 20°. The force and moment predictions are compared with experiments in Fig. 12. The results show that CFD and experiment data match well at 6°. They do not match everywhere at $\alpha = 20°$, particularly for the moment coefficients. Note that at 20° angle of attack, the wing vortices interact and merge and numerical and experimental results largely depend on the runtime. Figure 12 shows that while lateral coefficients (side-force, roll and yaw moments) are nearly linear with side-slip changes at $\alpha = 6°$, they become very nonlinear at $\alpha = 20°$. The high angle-of-attack data even show opposite slope signs in lateral coefficients.

Figure 13 shows the flow solution at extreme sideslip conditions and $\alpha = 6$ and 20°. Note that all vortex structures are asymmetric. At $\beta = 16°$ and $\alpha = 6°$, the fuselage vortex is shifted towards the left wing side. The canard and wing show much stronger vortices in the left side than the right side. The vortex cores are moved to the left as well. A vortex can also be seen over the left-side of the vertical tail originating from the tail apex. At $\beta = 16°$ and $\alpha = 20°$, the right wing vortices interact and merge to a single large vortex. However, no merged vortex can be seen on the left wing.

To investigate the effects of the gap regions in the overset mesh on solutions, CFD data from the single and overset meshes are compared for an angle-of-attack sweep. Figure 14 shows that these data are very close, though the overset mesh was only run for 2,000 iterations. Figure 11 also compares the surface solution of both meshes at 20 degrees angle of attack. Solutions of both meshes look similar; the overset mesh predicts a slightly larger canard vortex than the single mesh.

The overset mesh was then used to investigate and validate CFD data at different canard angles. These angles include $\phi_c = [-30°, -10°, 0°, 10°]$. The normal force and pitch moment coefficients were compared with available experimental data in Fig. 16. The results show that predictions from CFD using an overset grid method match very well with experiments. Note that the normal force and pitch moment increase with increasing canard angle. The curve slopes are similar for small angles of attack, but they become nonlinear with respect to canard angle at higher angles of attack. The canard effects on the TCR flowfield can be seen in Fig. 17 at 20 degrees angle of attack. As the canard angle decreases, the canard vortex becomes smaller and therefore the fuselage and LE vortex become larger. Notice that at $\phi_c = -30°$, no vortex is seen over the canard.

American Institute of Aeronautics and Astronautics

Final results correspond to validation of CFD data for forced-harmonic pitching motions. These motions are large amplitude motions defined as: $\alpha = 8° + 10°\sin(\omega t)$ and $\alpha = 8° + 20°\sin(\omega t)$ with frequencies of 0.5, 1.0, and 1.5 Hz. CFD solutions are compared with experiments in Figs. 18 and 19. The plots show that hysteresis loops are formed in the normal force and pitch moment curves. The plots also show that the hysteresis loops have nonlinear shape and they become bigger as the frequency increases. Even for these unsteady motions in nonlinear angle-of-attack regime, a good agreement was found between CFD and experiments.

VIII.   Conclusions

This work presented the CFD study of a canard-configured TransonicCruiser. The low speed aerodynamic characteristics of the TCR are available from the SimSAC project and were used in this work to validate CFD predictions. All tests were run at a value of free-stream velocity of 40 m/s, which corresponds to a sea level Mach number of 0.117, and a Reynolds number of 0.778 million based on the mean aerodynamic chord of the wind tunnel model. The TCR wind tunnel experiments only include total integrated forces/moments; the surface pressure measurements and flowfield information are not available from these tests.

An overset grid method was used to simulate canard deflections available in the experiments, however, a gap region is required between the canard (overset mesh) and the aircraft (background mesh) to allow the mesh assembly. CFD results show that the gap does not significantly affect the aerodynamic predictions. Numerical data with and without canard were compared with static and dynamic experimental data. Overall, a good agreement was found between CFD and experiments for most cases. The CFD data showed a dip in longitudinal coefficients between $\alpha = 18°$ and $\alpha = 24°$, but not the experiments. This dip becomes smaller for a canard-configured TCR. The occurrence of these dips depends on the simulation run time; dips could not be seen for short run simulations. Other discrepancies between CFD and experiment were seen in the sideslip angle sweeps at $\alpha = 20°$.

Flowfield solutions showed that vortices are formed over the wing, LEX, and fuselage of canardless TCR at moderate to high angles of attack. The wing vortex starting point becomes fixed at the wing apex; it moves toward the LEX vortex as the angle of attack increases. At about $\alpha = 20°$, the wing and LEX vortices interact and merge. For angles between $\alpha = 18°$ and $\alpha = 24°$, the merging point changes and then is nearly fixed at higher angles. The dip seen in the coefficients was related to the wing vortices interaction and merging. At high angles of attack, the fuselage vortex interacts with the wing vortices as well. For a canard-configured TCR, a vortex is formed over the canard that changes the wing/fuselage vortices and aerodynamic performance. The canard downwash causes smaller LEX and fuselage vortices. At high angles of attack, however, the canard vortex produces stronger merged vortices which increases the maximum lift and delays the vortex breakdown.

IX.   Acknowledgements

References

[1] Rizzi, A., Eliasson, P., Goetzendorf-Grabowski, T., Vos, J. B., Zhang, M., and Richardson, T. S., "Design of a Canard Configured TransCruiser Using CEASIOM," *Progress in Aerospace Sciences*, Vol. 47, No. 8, 2011, pp. 695–705 DOI :10.1016/j.paerosci.2011.08.011.

[2] Mani, M., Rider, B. J., Sclafani, A. J., Winkler, C., Vassberg, J., Dorgan, A. J., Cary, A., and Tinoco, E. N., "Reynolds-Averaged NavierStokes Technology for Transonic Drag Prediction: A Boeing Perspective," *Journal of Aircraft*, Vol. 51, No. 4, 2014, pp. 1118–1134 DOI :10.2514/1.C032717.

[3] Rizzi, A., P., E., McFarlane, C., Goetzendorf-Grabowski, T., and Vos, J., "Virtual-Aircraft Design & Control of TransCruiser a Canard Configuration," AIAA Paper 2010-8245, August 2010.

[4]Von Kaenel, R., Rizzi, A., Oppelstrup, J., Grabowski, T., Ghoreyshi, M., Cavagna, L., and Bérard, A., "CEASIOM: Simulating Stability & Control with CFD/CSM in Aircraft Conceptual Design," 26th International Congress of the Aeronautical Sciences, ICAS, 14 - 19 September 2008, Anchorage, Alaska, USA.

[5]Eliasson, P., DaRonch, A., Vos, J. B., Zhang, M., and Rizzi, A., "Virtual Aircraft Design of TransCruiser Computing Break Points in Pitch Moment Curve," AIAA Paper 2010-4366, June-July 2010.

[6]Da Ronch, A., Vallespin, D., Ghoreyshi, M., and Badcock, K. J., "Evaluation of Dynamic Derivatives Using Computational Fluid Dynamics," *AIAA Journal*, Vol. 50, No. 2, 2012, pp. 470484
DOI :10.2514/1.J051304.

[7]Samimi, S., Davari, A. R., and Soltani, M. R., "Canard-Wing Interactions in Subsonic Flow," *IJST, Transactions of Mechanical Engineering*, Vol. 37, No. 2, 2013, pp. 133–147.

[8]Khrabrov, A., Kolinko, K., Zhuk, A., and Grishin, I., "Wind Tunnel Test Report," SimSAC Technical Report, October 2009.

[9]Er-El, J., "Effect of Wing/Canard Interference on the Loading of a Delta Wing," *Journal of Aircraft*, Vol. 25, No. 1, 1988, pp. 18–24
DOI :10.2514/3.45535.

[10]Torenbeek, E., *Synthesis of Subsonic Airplane Design*, Delft University Press, Netherlands, 1982.

[11]Gloss, B. B. and McKmney, L. W., "Canard Wing Lift Intereference Related to Maneuvering Aircraft At Subsonic Speeds," NASA Technical Report, NASA TM X-2897, December 1973.

[12]Phillips, W. F., *Mechanics of Flight*, Aerospace/Engineering, Wiley, 2004.

[13]Zhang, G. Q., Yu, S. C. M., Chien, A., and Yang, S. X., "Aerodynamic Characteristics of Canard-Forward Swept Wing Aircraft Configurations," *Journal of Aircraft*, Vol. 50, No. 2, 2013, pp. 378–387
DOI :10.2514/1.C031740.

[14]Fleeman, E. L., *Tactical Missile Design*, AIAA education series, American Institute of Aeronautics and Astronautics, 2006.

[15]Roskam, J., "Airplane Design," 1990, Roskam Aviation and Engineering Corporation, Kansas, USA.

[16]Tu, E. L., "Effect of Canard Deflection on Closed-Coupled Canard-Wing-Body Aerodynamics," *Journal of Aircraft*, Vol. 31, No. 1, 1994, pp. 138–145
DOI :10.2514/3.46466.

[17]O'leary, J. F., *Flowfield Study of a Close-Coupled Canard Configuration*, Master's thesis, Naval Postgraduate School, June 1992.

[18]Pamadi, B. N., *Performance, Stability, Dynamics, and Control of Airplanes*, AIAA Education Series, AIAA, Reston, Virginia, 2004.

[19]Rom, J., *High Angle of Attack Aerodynamics: Subsonic, Transonic, and Supersonic Flows*, Springer New York, 2012.

[20]Bergamnn, A. and Hummel, D., "Aeodynamic Effects of Cnard Position On a Wing Body Configuration In Symmetrical Flow," AIAA Paper 2001-0116, January 2001.

[21]Thomas, J. L., Krist, S. T., and Anderson, W. K., "Navier-Stokes Computations of Vortical Flows Over Low-Aspect-Ratio Wings," *AIAA Journal*, Vol. 28, No. 2, 1990, pp. 205–212
DOI :10.2514/3.10376.

[22]Gursul, I., Gordnier, R., and Visbal, M., "Unsteady Aerodynamics of Nonslender Delta Wings," *Progress in Aerospace Sciences*, Vol. 41, No. 7, 2005, pp. 515–557
DOI :10.1016/j.paerosci.2005.09.002.

[23]Tyssel, L., "Hybrid Grid Generation for Complex 3D Geometries," Proceedings of the 7th International Conference on Numerical Grid Generation in Computational Field Simulation, 2000, pp. 337–346.

[24]Tyssel, L., "The TRITET Grid Generation System," International Society of Grid Generation (ISGG)," Proceedings of the 10the International Conference on Numerical Grid Generation in Computational Field Simulations, 2000.

[25]Strang, W. Z., Tomaro, R. F., and Grismer, M. J., "The Defining Methods of Cobalt: A Parallel, Implicit, Unstructured Euler/Navier-Stokes Flow Solver," AIAA Paper 1999–0786, 1999.

[26]Gottlieb, J. J. and Groth, C. P. T., "Assessment of Riemann Solvers For Unsteady One-dimensional Inviscid Flows of Perfect Gasses," *Journal of Fluids and Structure*, Vol. 78, No. 2, 1998, pp. 437–458
DOI :10.1016/0021–9991(88)90059–9.

[27]Tomaro, R. F., Strang, W. Z., and Sankar, L. N., "An Implicit Algorithm For Solving Time Dependent Flows on Unstructured Grids," AIAA Paper 1997–0333, 1997.

[28]Spalart, P. R. and Allmaras, S. R., "A One Equation Turbulence Model for Aerodynamic Flows," AIAA Paper 1992–0439, January 1992.

[29]Wilcox, D. C., "Reassesment of the Scale Determining Equation for Advanced Turbulence Models," *AIAA Journal*, Vol. 26, No. 11, 1988, pp. 1299–1310
DOI :10.2514/3.1004.

[30]Menter, F., "Eddy Viscosity Transport Equations and Their Relation to the $k - \varepsilon$ Model," *ASME Journal of Fluids Engineering*, Vol. 119, 1997, pp. 876–884
DOI: 10.1115/1.2819511.

[31]Tuncer, I. H., Gulcat, U., Emerson, D. R., and Matsuno, K., *Parallel Computational Fluid Dynamics 2007*, Springer-Verlag,Germany, 2009.
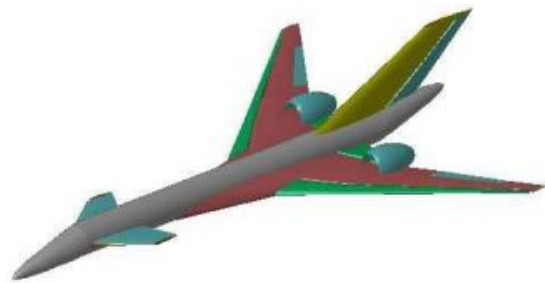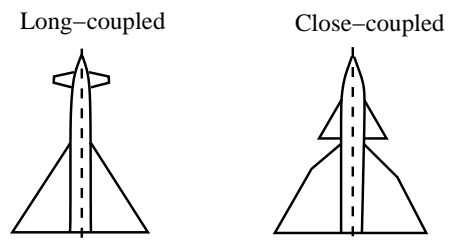
(a) TCR design concept[1]

(b) TCR wind tunnel model[8]

Figure 1. TCR design and wind tunnel model.

Long–coupled   Close–coupled

Figure 2. Canard types. Adapted from Ref. 17

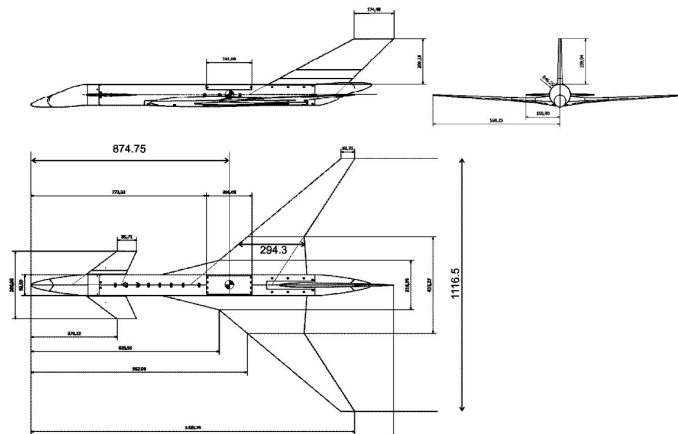American Institute of Aeronautics and Astronautics

Figure 3. TCR wind tunnel model schematic.[8]
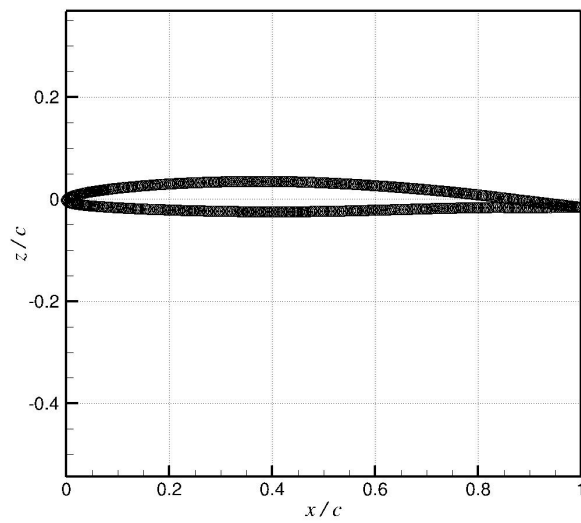
Figure 4. TCR wing airfoil section at $Y = 0.3m$.

American Institute of Aeronautics and Astronautics

(a) without canard

(b) with canard
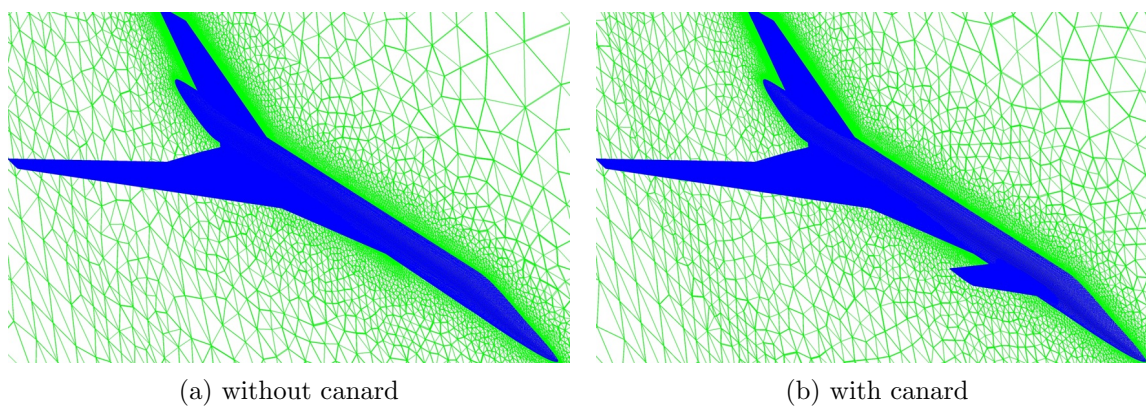
Figure 5. TCR single meshes.

(a) canard mesh overset to the background mesh

(b) ϕ_c=-30°
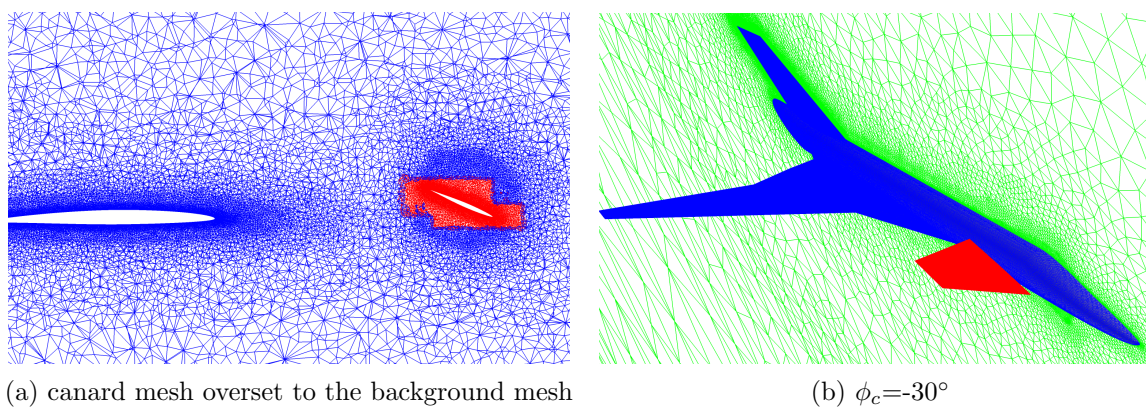
Figure 6. TCR overset mesh.

(a) normal-force coefficient

(b) pitch-moment coefficient

(c) Drag coefficient

(d) Normal force changes with number of iterations
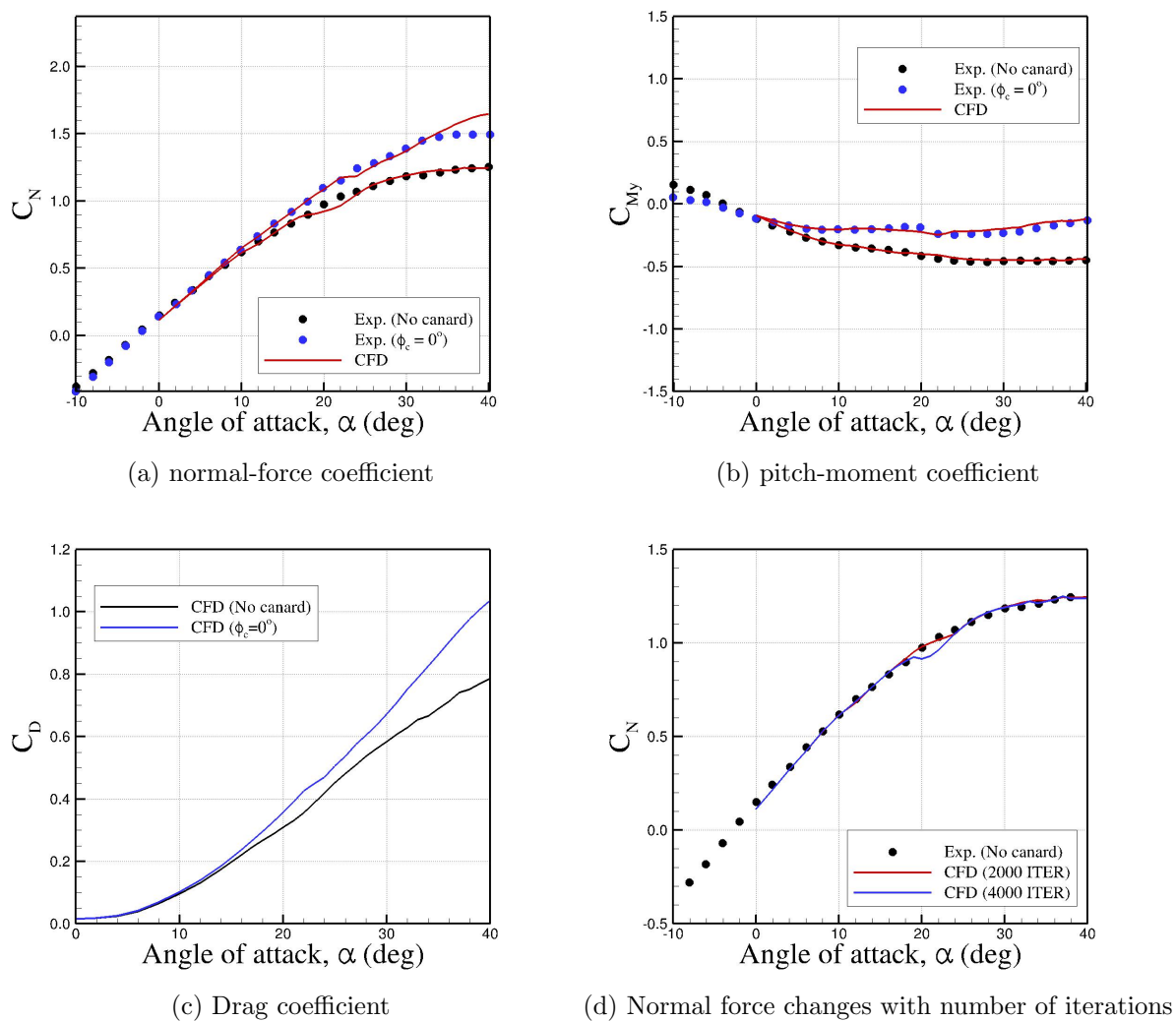
Figure 7. Sweeps of angle of attack with and without canard. All meshes are single grids.

(a) normal-force coefficient

(b) pitch-moment coefficient

(c) Drag coefficient
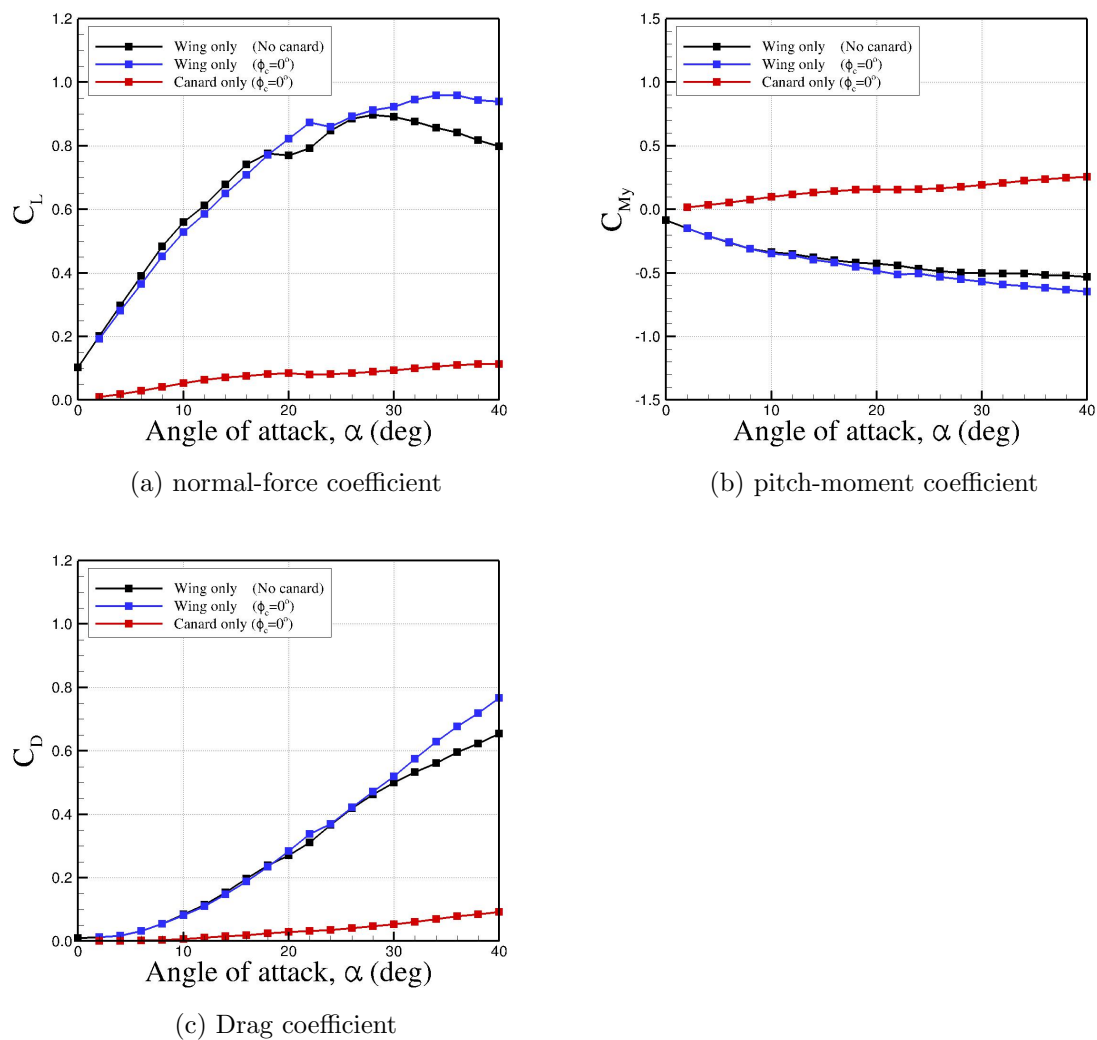
Figure 8. Effects of canard on the wing aerodynamic performance.

American Institute of Aeronautics and Astronautics

(a) $\alpha = 6°$

(b) $\alpha = 12°$

(c) $\alpha = 18°$

(d) $\alpha = 24°$

(e) $\alpha = 30°$

(f) $\alpha = 40°$
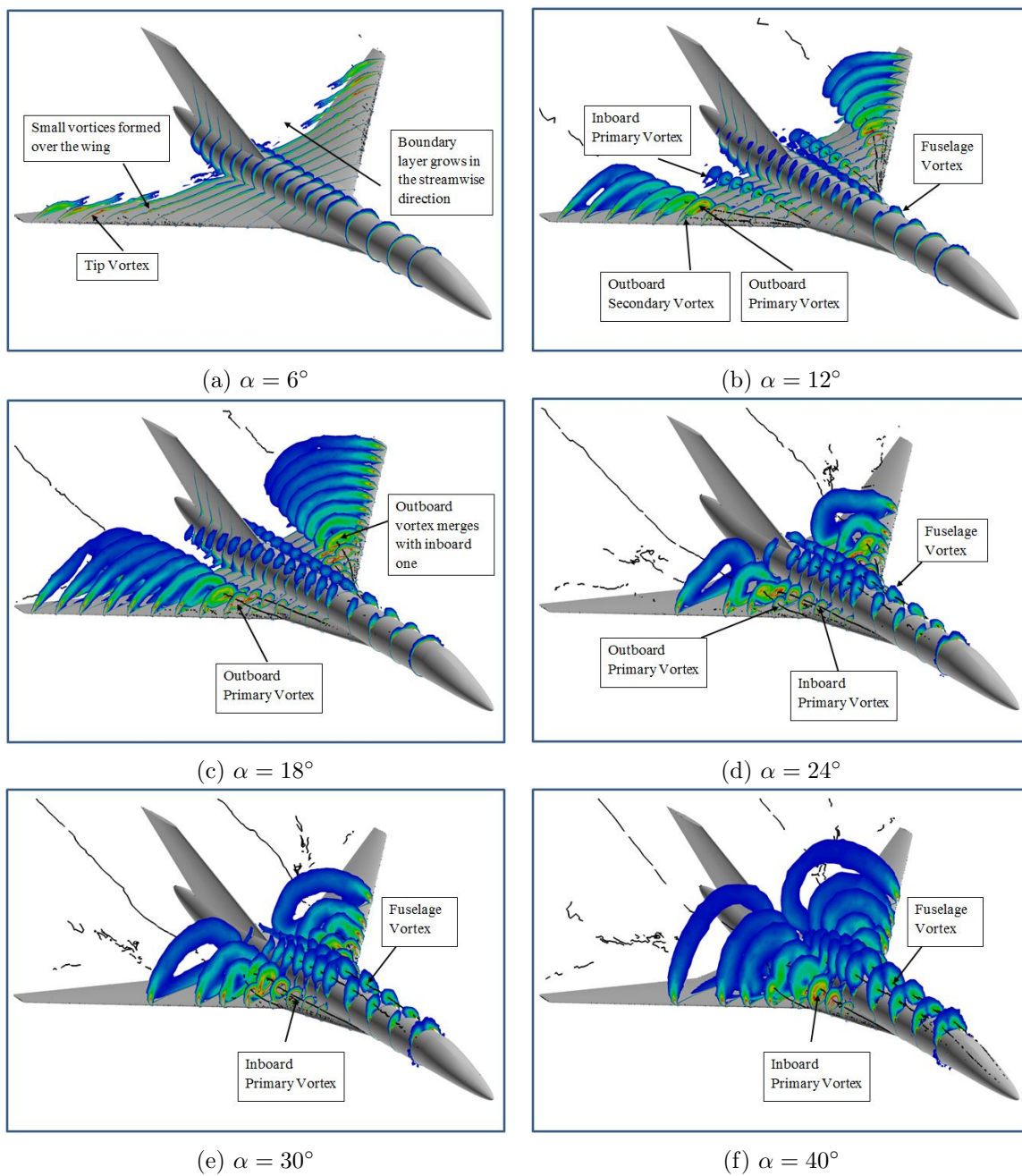
Figure 9. TCR (without canard) flow solutions. Iso-surfaces were created and colored by vorticity. The black lines show the core of vortices.
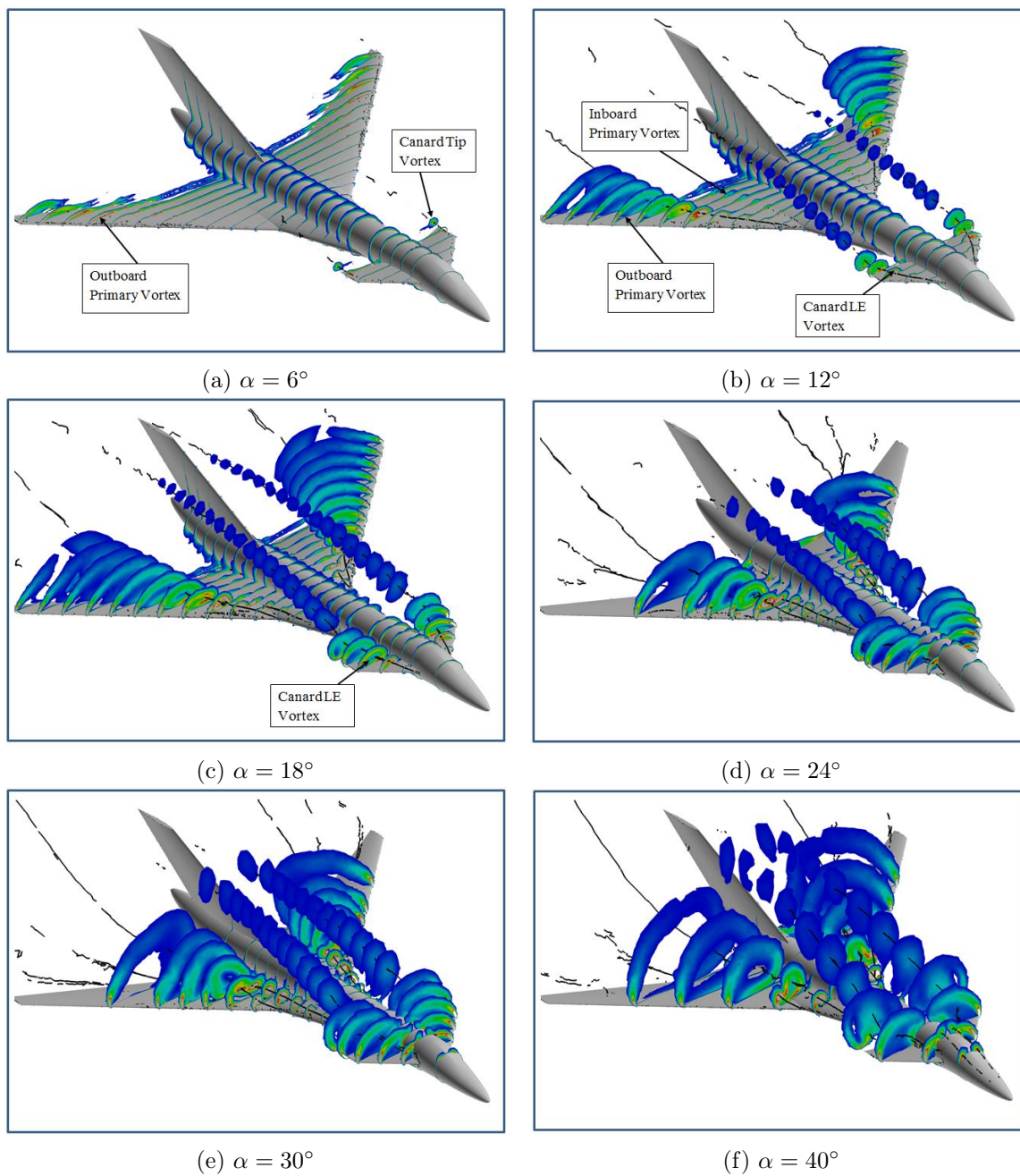
(a) $\alpha = 6°$

(b) $\alpha = 12°$

(c) $\alpha = 18°$

(d) $\alpha = 24°$

(e) $\alpha = 30°$

(f) $\alpha = 40°$

Figure 10. TCR ($\phi_c = 0°$) flow solutions. Iso-surfaces were created and colored by vorticity. The black lines show the core of vortices.
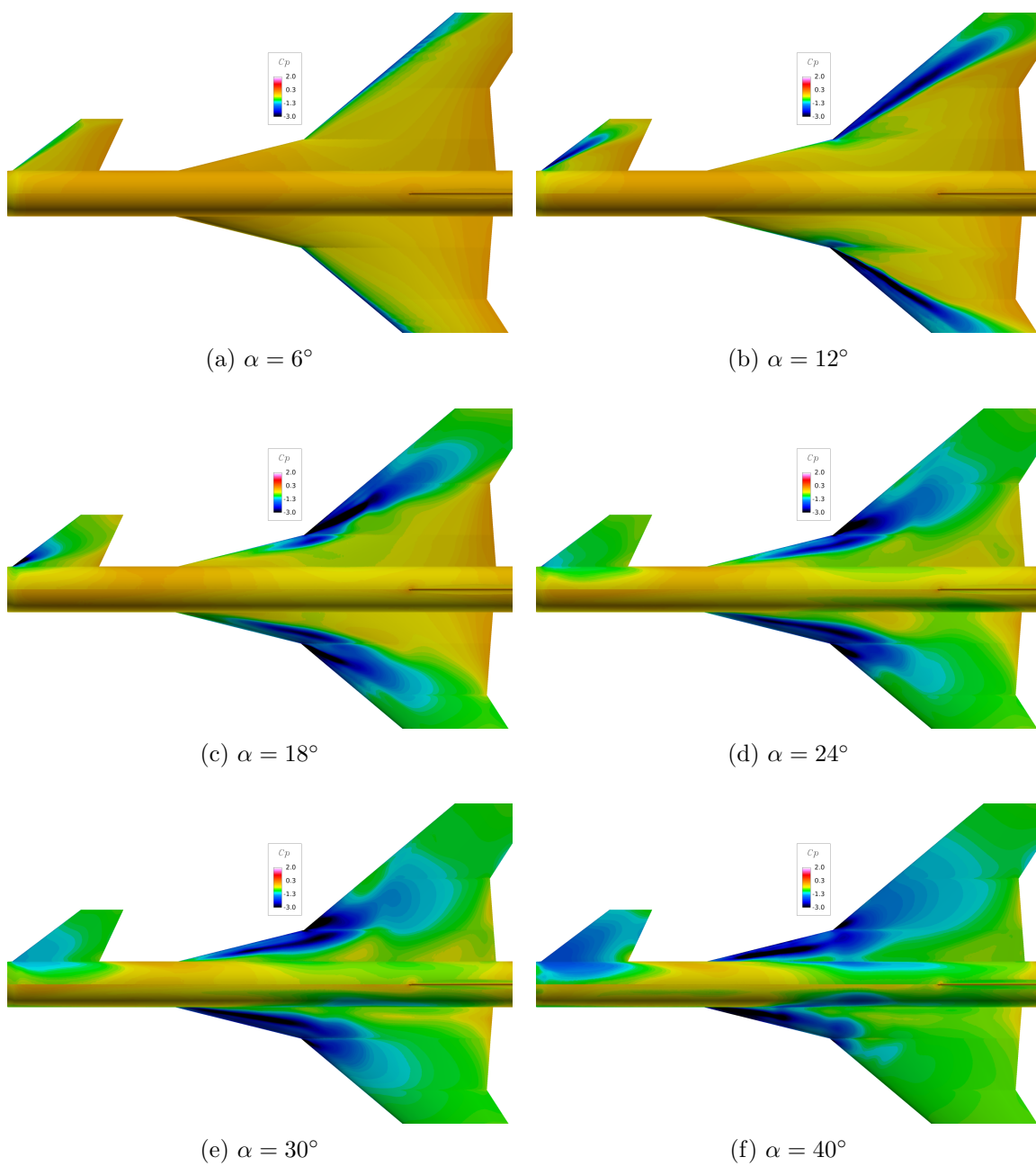
American Institute of Aeronautics and Astronautics

(a) $\alpha = 6°$

(b) $\alpha = 12°$

(c) $\alpha = 18°$

(d) $\alpha = 24°$

(e) $\alpha = 30°$

(f) $\alpha = 40°$

Figure 11. Canard on/off pressure solutions.

American Institute of Aeronautics and Astronautics

(a) normal-force coefficient

(b) pitch-moment coefficient

(c) side-force coefficient

(d) roll-moment coefficient

(e) Yaw-moment coefficient
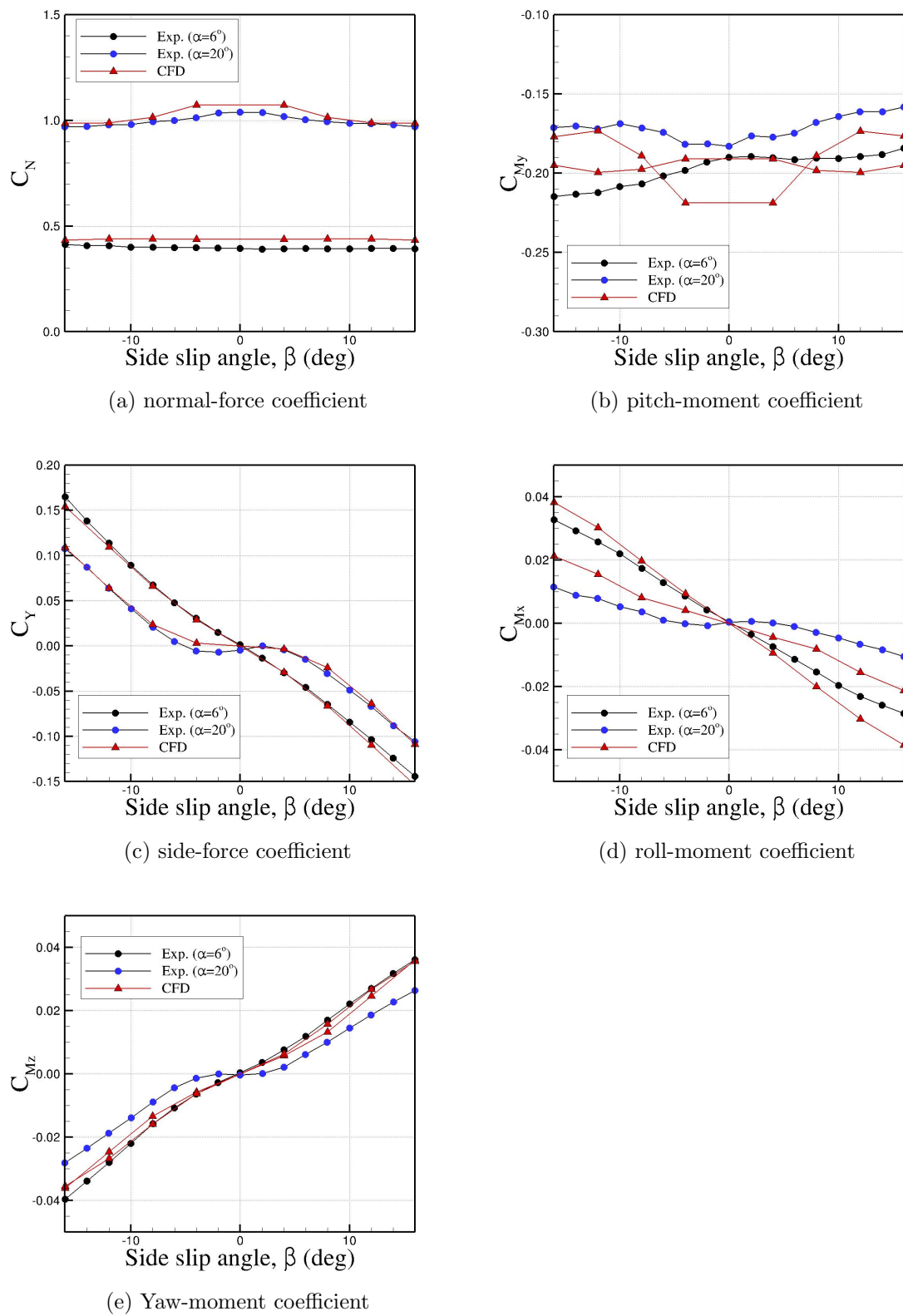
Figure 12. Sweeps of side-slip for $\alpha = 6°$ and $\alpha = 20°$ and $\phi_c = 0°$

American Institute of Aeronautics and Astronautics

(a) $\alpha = 6°$ and $\beta = -16°$

(b) $\alpha = 20°$ and $\beta = -16°$

(c) $\alpha = 6°$ and $\beta = 16°$

(d) $\alpha = 20°$ and $\beta = 16°$
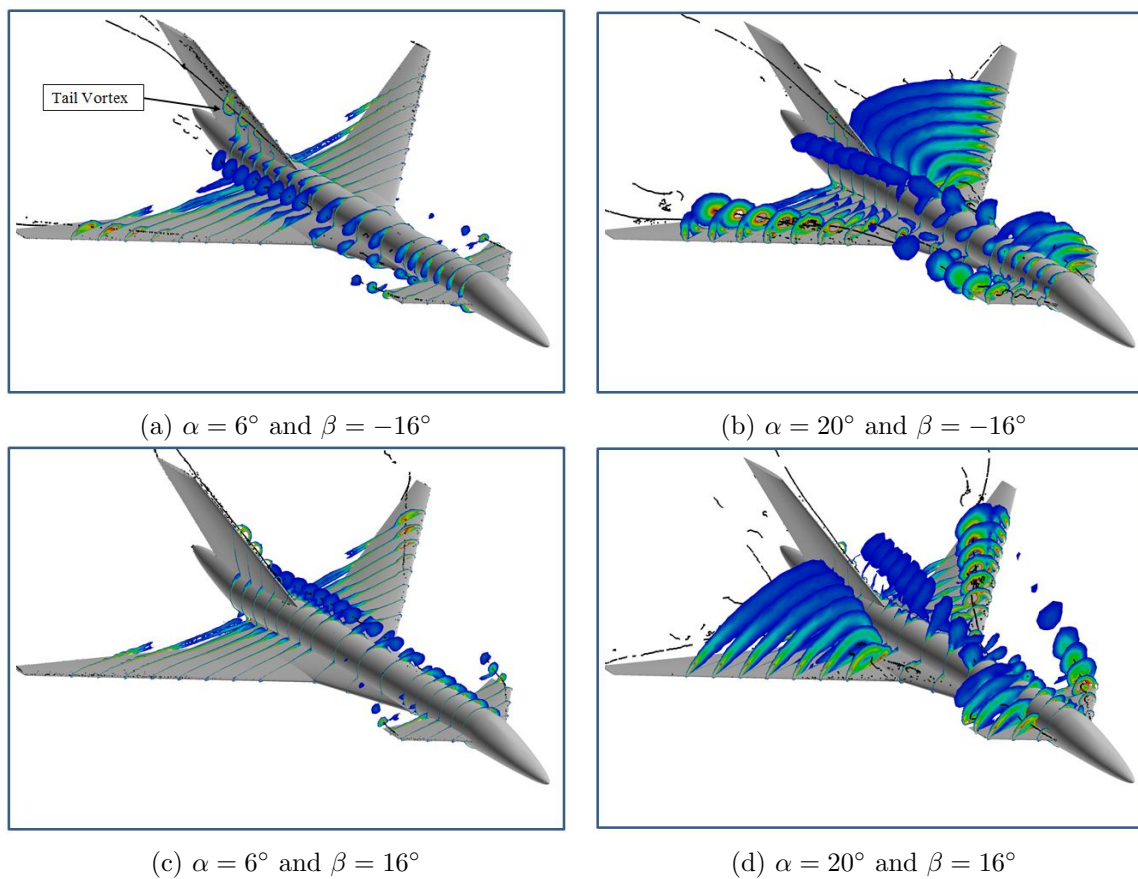
Figure 13. TCR ($\phi_c = 0°$) flow solutions at sideslip angles. Iso-surfaces were created and colored by vorticity. The black lines show the core of vortices.

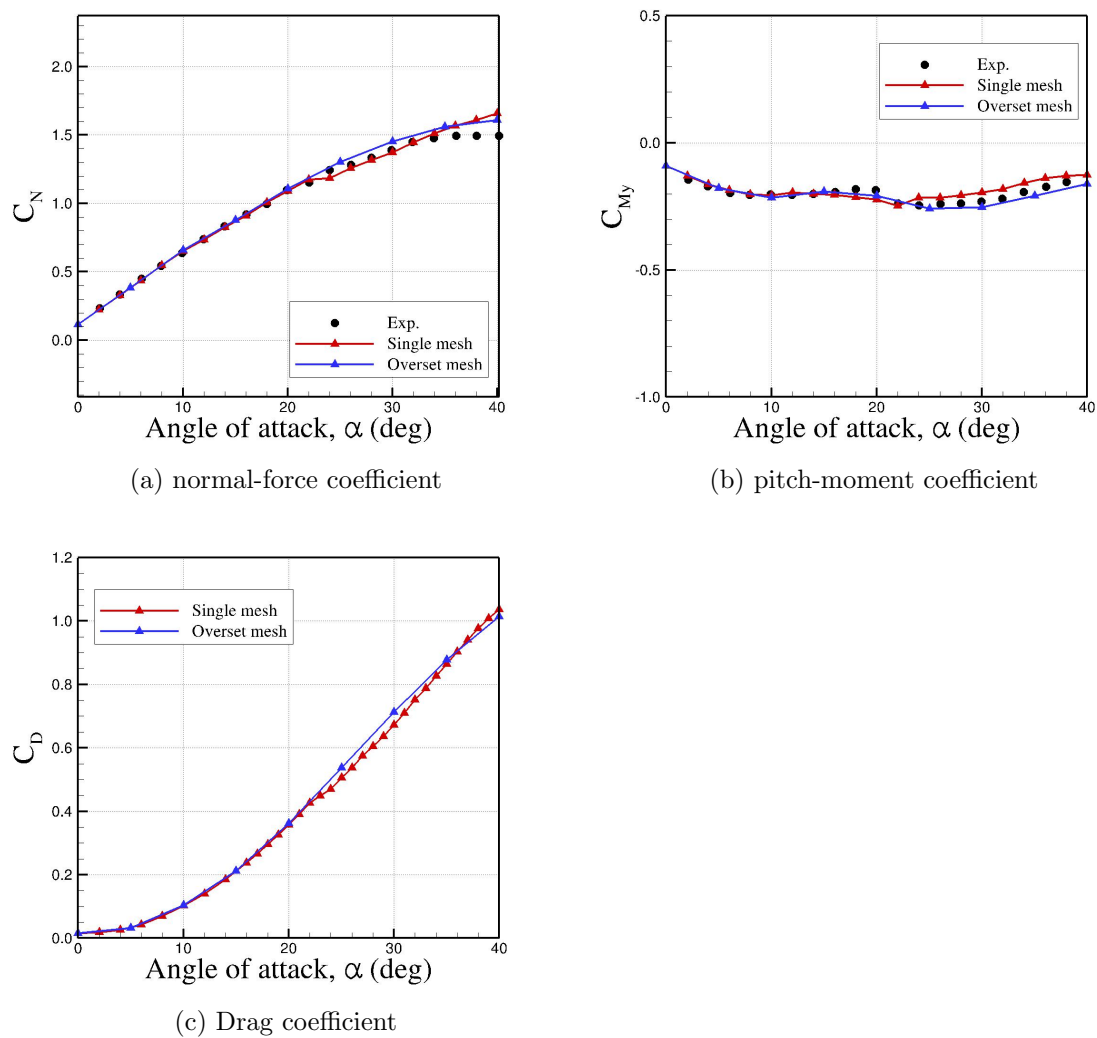American Institute of Aeronautics and Astronautics

(a) normal-force coefficient

(b) pitch-moment coefficient

(c) Drag coefficient

Figure 14. Comparison of single and overset mesh prediction at $\phi_c = 0°$.
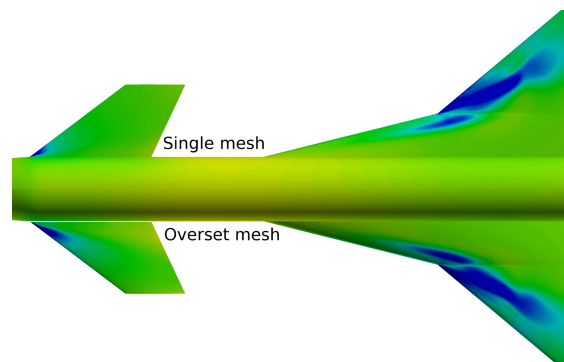
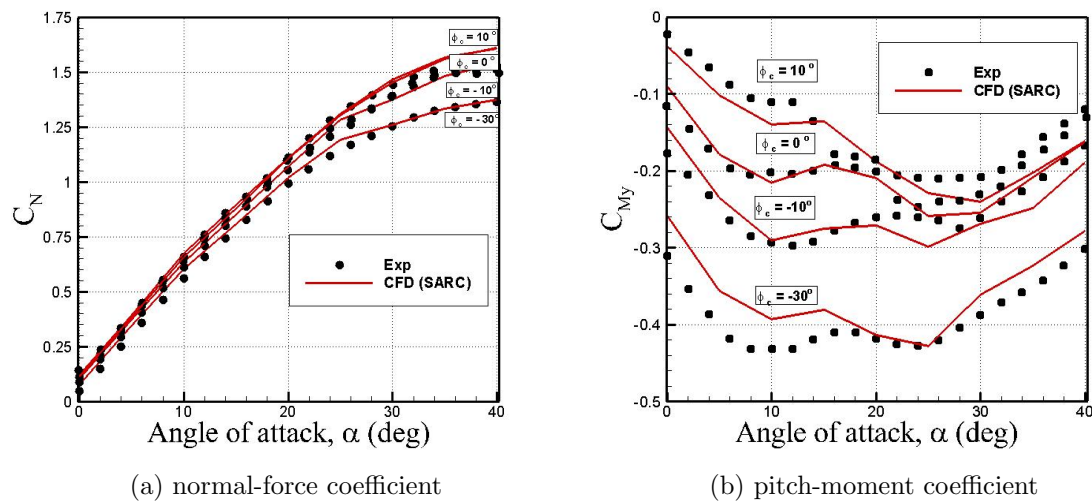**Figure 15. Effects of the canard gap on the overset flow predictions. $\alpha = 20°$ and $\phi_c = 0°$.**

American Institute of Aeronautics and Astronautics

(a) normal-force coefficient

(b) pitch-moment coefficient

Figure 16. Validation of the overset mesh for canard deflections of $\phi_c = -10°, 0°, 10°,$ and $30°$.

(a) $\phi_c = 10°$
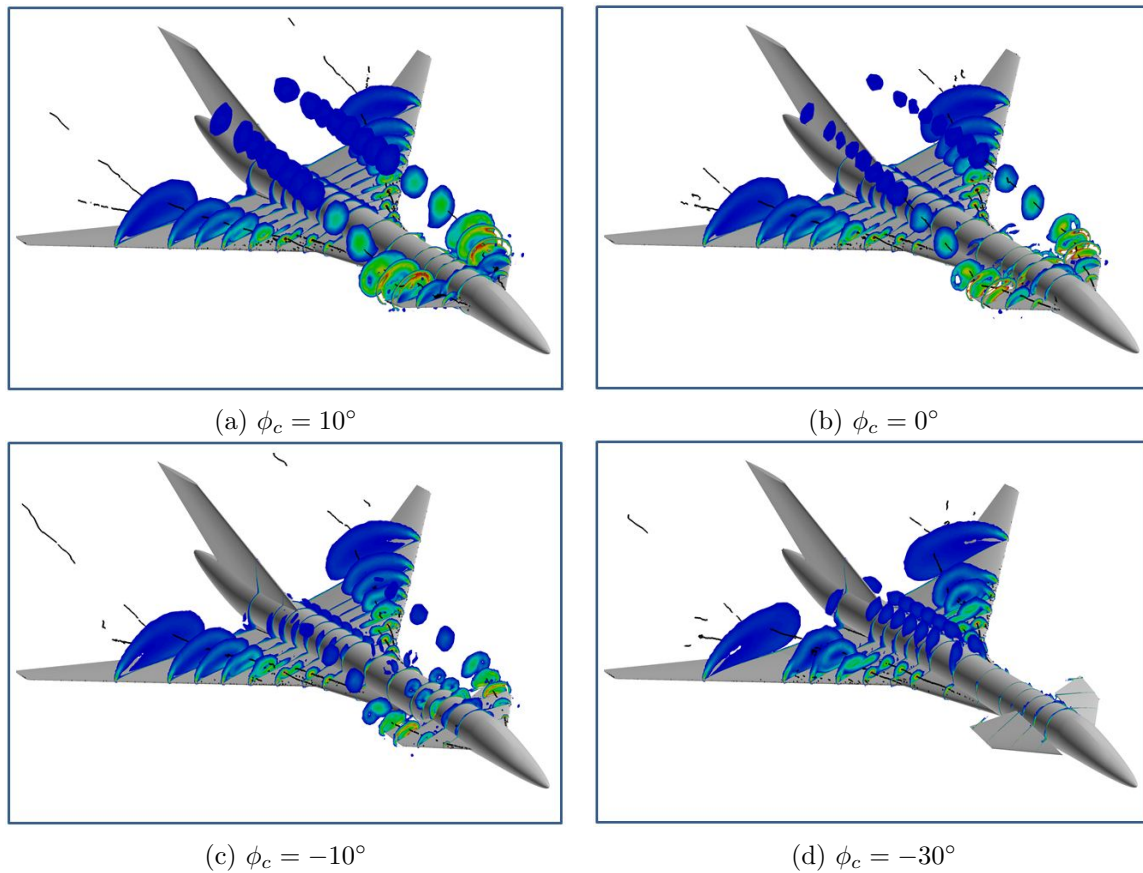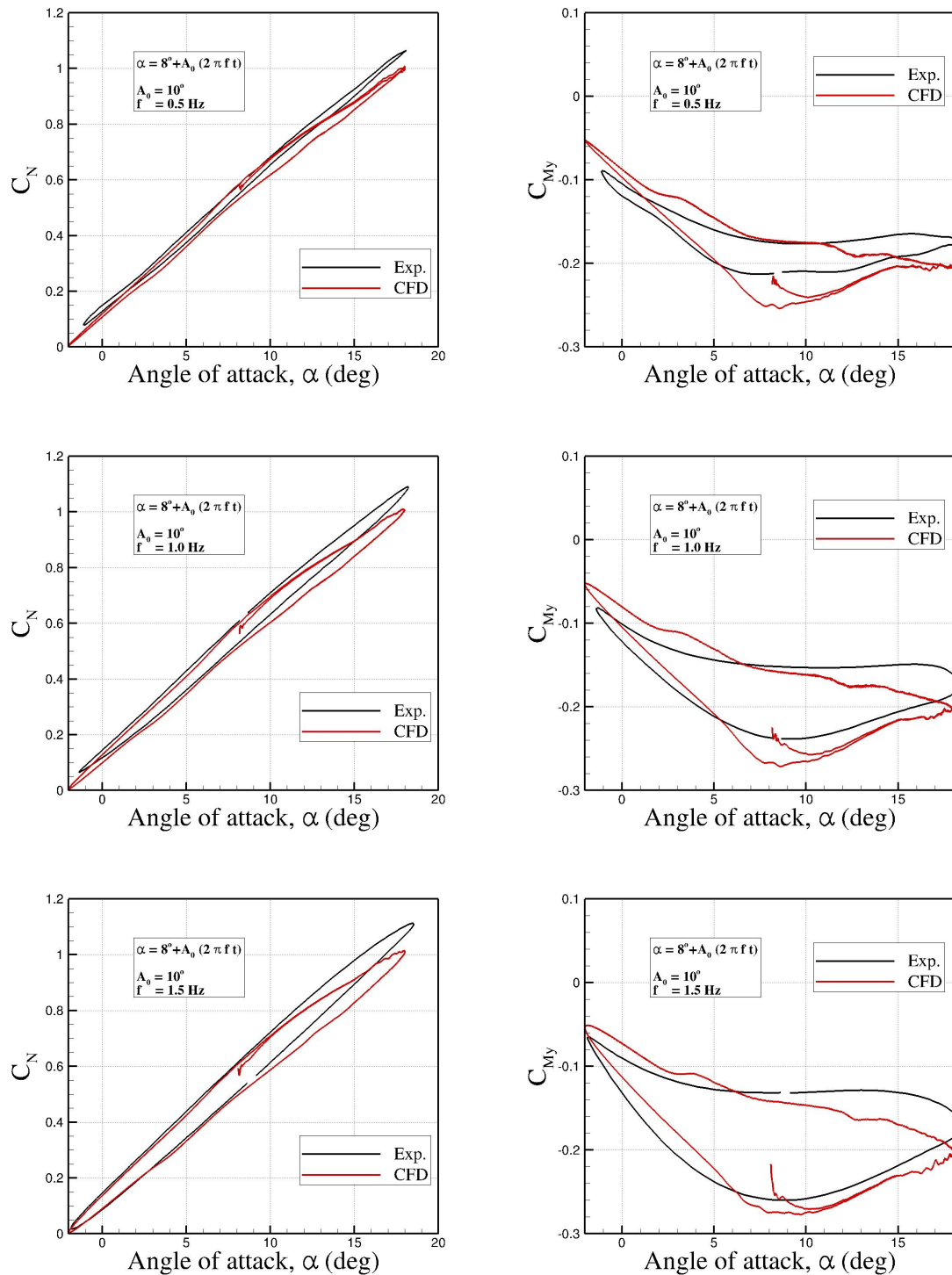
(b) $\phi_c = 0°$

(c) $\phi_c = -10°$

(d) $\phi_c = -30°$

Figure 17. TCR flow solutions at $\alpha = 20°$ for different canard deflections. Iso-surfaces were created and colored by vorticity. The black lines show the core of vortices.

Figure 18. **Validation of forced oscillation motions at** $\phi_c = 0°$. **The motions are defined as** $\alpha = 8° + 10°\sin(2\pi f t)$ **with** $f =$**0.5, 1.0, and 1.5 Hz.**
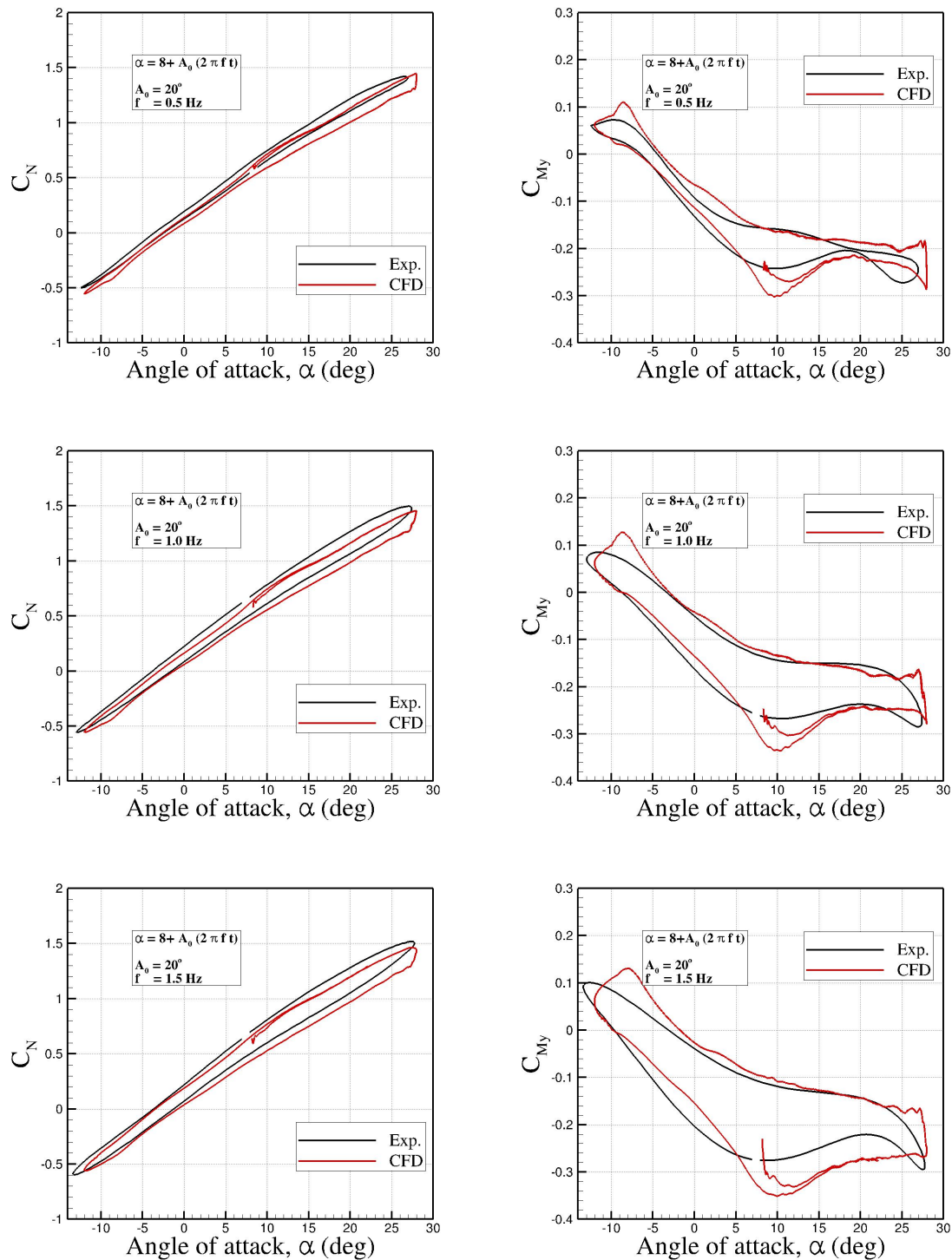
American Institute of Aeronautics and Astronautics

Figure 19. Validation of forced oscillation motions at $\phi_c = 0°$. The motions are defined as $\alpha = 8° + 20°\sin(2\pi f t)$ with $f =$0.5, 1.0, and 1.5 Hz.

American Institute of Aeronautics and Astronautics